An Overlapping Subzone Technique for MR-Based Elastic Property Reconstruction

E.E.W. Van Houten,[1]* K.D. Paulsen,[1,2,3] M.I. Miga,[1] F.E. Kennedy,[1] and J.B. Weaver[2]

A finite element–based nonlinear inversion scheme for magnetic resonance (MR) elastography is detailed. The algorithm operates on small overlapping subzones of the total region of interest, processed in a hierarchical order as determined by progressive error minimization. This zoned approach allows for a high degree of spatial discretization, taking advantage of the data-rich environment afforded by the MR. The inversion technique is tested in simulation under high-noise conditions (15% random noise applied to the displacement data) with both complicated user-defined stiffness distributions and realistic tissue geometries obtained by thresholding MR image slices. In both cases the process has proved successful and has been capable of discerning small inclusions near 4 mm in diameter. Magn Reson Med 42:779–786, 1999. © 1999 Wiley-Liss, Inc.

Key words: elasticity reconstruction; nonlinear inversion; finite element method; magnetic resonance elastography; subzone technique; model-based imaging

The diagnostic value of tissue elasticity has long been appreciated in a broad spectrum of medical applications, and understanding of its importance continues to grow. From pathology detection (1,2), to robotic surgery (3,4), to the use of computational modeling during surgical procedures (5–7), a demand for detailed and accurate tissue elasticity information has been generated. Recent research into the use of mechanical properties of biological tissue for clinical decision making has moved away from direct mechanical measurements (8,9) and turned toward various medical imaging technologies to assess tissue behavior under mechanical loads. The idea of ultrasound elastography has been introduced (10–16) in which some form of ultrasonic displacement measurement technique is used to detect subsurface tissue motion. This displacement information can then be correlated to the elastic property distribution in the tissue with the aid of a model for tissue motion as a function of shear or Young's modulus (17–19).

Ultrasound's inherent lack of lateral resolution and limited axial resolution when compared with other clinically available imaging modalities has motivated the development of magnetic resonance (MR) elastography methods (20–22). MR offers the potential of generating highly resolved, three-dimensional (3D) information with relative ease, as opposed to the considerable challenge associated with obtaining equivalent data from ultrasound techniques. However, given the availability of finely sampled 3D displacement fields, the task of developing a robust algorithm capable of deducing elastic property distributions from these displacement images while maintaining the refinement of the MR data remains.

Strategies for addressing the reconstruction problem have varied widely to date. Chenevert et al. are investigating MR elastography through a quasistatic displacement approach (23), whereas Raghavan and Yagle have developed an inversion technique based on a finite difference formulation of the global elasticity equations (24). A collaboration between Lewa and De Certaines has attempted to determine the viscoelastic properties directly from MR measurements (25). Manduca et al. have developed an inversion scheme based on a local frequency estimation that is correlated to a local elasticity value (26), and Sumi and Nakayama have presented a method for numerically integrating the two-dimensional (2D) stress-strain relations to reconstruct a shear modulus distribution from strain measurements (27).

In this report, we present a finite element–based method for solving the elastography inversion problem by use of a least-squares minimization of the difference between measured displacement data from the MR and computed displacement solutions. Our approach is not unlike that recently presented by Kallel and Bertrand for ultrasound techniques (18), except that model-based optimization is performed on small overlapping subzones of the total tissue region of interest that are processed in an hierarchical order determined by progressive error minimization. This is a significant shift in the conceptual framework for property inversion that allows the recovery of an elasticity distribution at the MR displacement measurement resolution. Property estimation at the MR pixel level is not computationally viable as a single global minimization problem; however, the subzone approach we have identified eliminates this limitation by recasting the image reconstruction objective as a sum of minimizations rather than a single minimization of sums. The results show that the overlapping zone concept is robust with respect to simulated measurement noise and that local minimization of the least-squares match between the model and the MR displacement data leads to high-quality global property distribution images.

SUBZONE INVERSION

Our approach capitalizes on recent advances in model-based image reconstruction of tissue properties whereby the nonlinear relationship between the physical property distribution to be determined and the measured tissue response to an applied stimulus is preserved (28–30). Specifically, we formulate the MR elastography image-reconstruction problem as a constrained optimization task
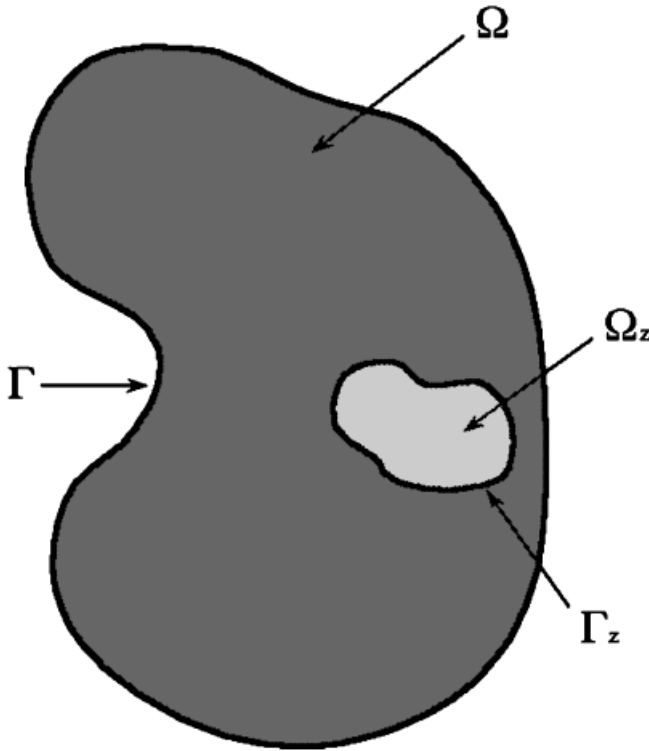
FIG. 1. Schematic diagram of the subzone concept. Ω, total problem domain; Γ, boundary; Ω_z, single subzone domain; Γ_z, single subzone boundary.

whose objective is to minimize the difference between a set of measured displacement fields and those computed by a model description in which the tissue property distribution is parameterized as a set of unknown coefficients. The typical strategy is to define a single objective to be minimized that is the sum of the squared differences between measured and calculated quantities over the entire set of tissue response observations that are available (31):

$$\min F(E), \qquad [1a]$$

where

$$F(E) = \sum_{l=1}^{N} (u_l^m - u_l^c)^2 + (v_l^m - v_l^c)^2 \qquad [1b]$$

and u_l^m and v_l^m are the x and y vector components of the measured displacement at location l, while u_l^c and v_l^c are the calculated vector components at the same position, for a total of N different locations. E is the M-dimensional vector of elasticity parameters that is expanded on a continuous basis set, ϕ, to define the tissue property distribution of the total region of interest, Ω.

This total problem domain, Ω, may be thought of as the union of multiple "subzones," Ω_z, of the total ROI, as illustrated in Fig. 1, so that we may rewrite the global functional, $F(E)$, as a sum of locally defined functionals,

$F_z(E_z)$, for the zth subzone. For Q subzones,

$$F(E) = \sum_{z=1}^{Q} F_z(E_z), \qquad [2]$$

where the minimization of the sum is replaced by the sum of minimizations on the individual subzones:

$$\min F(E) = \min \left\{ \sum_{z=1}^{Q} F_z(E_z) \right\} \Rightarrow \sum_{z=1}^{Q} \min F_z(E_z) \} \qquad [3a]$$

with

$$F_z(E_z) = \sum_{l_z=1}^{N_z} (u_{l_z}^m - u_{l_z}^c)^2 + (v_{l_z}^m - v_{l_z}^c)^2, \qquad [3b]$$

when each subzone consists of N_z tissue response observations and M_z tissue property parameters such that $N_z \ll N$ and $M_z \ll M$.

The advantages of this approach are severalfold. First, the nonlinear minimization process occurs on only M_z tissue property parameters using N_z observations at a time. The significant reduction in the size of the inversion problem is important because the least-squares approach scales cubically in the number of optimization parameters to be determined. Second, it maximizes the utilization of the complete MR displacement data set and the concomitant tissue property resolution that can be achieved. Assuming that tissue displacements can be measured at the MR pixel level, the total amount of tissue response data and tissue property values that could be recovered in a single minimization problem exceeds the computational resources available today. By dividing the problem into subzones, high-resolution (MR pixel-level) property maps can be deduced that take full advantage of the high density of tissue measurements that the MR technique provides.

Once defined on the subzone, the minimization problem proceeds in standard fashion. Determination of the subzone elastic properties requires differentiation of F_z in Eq. [3b] with respect to each of the M_z property parameters contained in E_z, which produces the nonlinear system

$$f_1 = \frac{\partial F_z}{\partial E_{z_1}} = \sum_{l_z=1}^{N_z} (u_{l_z}^m - u_{l_z}^c) \frac{\partial u_{l_z}^c}{\partial E_{z_1}} + \sum_{l_z=1}^{N_z} (v_{l_z}^m - v_{l_z}^c) \frac{\partial v_{l_z}^c}{\partial E_{z_1}} = 0$$

$$f_2 = \frac{\partial F_z}{\partial E_{z_2}} = \sum_{l_z=1}^{N_z} (u_{l_z}^m - u_{l_z}^c) \frac{\partial u_{l_z}^c}{\partial E_{z_2}} + \sum_{l_z=1}^{N_z} (v_{l_z}^m - v_{l_z}^c) \frac{\partial v_{l_z}^c}{\partial E_{z_2}} = 0$$

$$\vdots \quad \vdots \qquad\qquad\qquad \vdots$$

$$f_{M_z} = \frac{\partial F_z}{\partial E_{z_{M_z}}} = \sum_{l_z=1}^{N_z} (u_{l_z}^m - u_{l_z}^c) \frac{\partial u_{l_z}^c}{\partial E_{z_{M_z}}}$$

$$+ \sum_{l_z=1}^{N_z} (v_{l_z}^m - v_{l_z}^c) \frac{\partial v_{l_z}^c}{\partial E_{z_{M_z}}} = 0. \qquad [4]$$

Solution of this equation set by Newton's method leads to iterative improvements in the elastic property profile such that

$$E_z^{(n+1)} = E_z^n + \Delta E_z, \qquad [5a]$$

where ΔE_z is the property update vector determined from the solution of the regularized matrix system

$$[(\mathbf{H}_z^n + \alpha \mathbf{I})] \{\Delta E_z\} = \{-f_z^n\} \qquad [5b]$$

with $f_z = \{f_1^n, f_2^n, \ldots, f_{M_z}^n\}^T$ and the approximate Hessian matrix (second-order terms are dropped), $\mathbf{H}_z^n$, having the elements

$$h_{ij}^n = \frac{\partial f_i^n}{\partial E_{z_j}} = -\sum_{l_z=1}^{N_z} \left[\frac{\partial u_{l_z}^c}{\partial E_{z_i}^n} \frac{\partial u_{l_z}^c}{\partial E_{z_j}^n} + \frac{\partial v_{l_z}^c}{\partial E_{z_i}^n} \frac{\partial v_{l_z}^c}{\partial E_{z_j}^n} \right] \qquad [5c]$$

evaluated at the current property estimate denoted by the superscript *n*. In Eq. (5b), α is a scalar regularization parameter added to the diagonal of $\mathbf{H}$ to facilitate its inversion, because $\mathbf{H}$ is known to be poorly conditioned. This parameter is scaled to the subzone problem at hand by use of the Levenberg-Marquardt approach (32).

Solution of Eq. [5b] requires a vehicle for calculating the subzone displacement field and its derivatives with respect to each property parameter given the current estimate of the property distribution on the subzone. Here, we assume that the displacement field is described by the partial differential equation governing time-harmonic, isotropic, linearly elastic motion:

$$\nabla \cdot G\nabla \mathbf{u} + \nabla(\lambda + G)\nabla \cdot \mathbf{u} = -\rho\omega^2 \mathbf{u}, \qquad [6a]$$

where $\mathbf{u}$ is the displacement vector, ρ is the tissue density and G and λ are Lamé's constants

$$G = \frac{E}{(2 + 2\nu)} \qquad [6b]$$

$$\lambda = \frac{\nu E}{(1 + \nu)(1 - 2\nu)} \qquad [6c]$$

for Poisson's Ratio, ν, and Young's modulus, *E*. For simplicity, we consider ρ and ν to be known constants, leaving G, or equivalently E, as the elastic property parameter distribution to be estimated from the displacement field. To solve Eq. [6a], we use the finite element method as summarized in the Appendix.

The required derivatives are calculated by differentiating Eq. [6a] directly with respect to each property parameter, E_{z_j} for $j = 1, 2, \ldots, M_z$, and solving the resulting partial differential equation in the derivative quantity of interest

on the same finite element discretization:

$$\frac{\partial}{\partial E_{z_j}} [\nabla \cdot G\nabla \mathbf{u} + \nabla(\lambda + G)\nabla \cdot \mathbf{u} = -\rho\omega^2 \mathbf{u}]$$

$$= \nabla \cdot \frac{\partial G}{\partial E_{z_j}} \nabla \mathbf{u} + \nabla \cdot G\nabla \frac{\partial \mathbf{u}}{\partial E_{z_j}} + \nabla \frac{\partial}{\partial E_{z_j}} (\lambda + G)\nabla \cdot \mathbf{u}$$

$$+ \nabla(\lambda + G)\nabla \cdot \frac{\partial \mathbf{u}}{\partial E_{z_j}} = -\rho\omega^2 \frac{\partial \mathbf{u}}{\partial E_{z_j}}, \quad [7a]$$

which when rewritten in the form

$$\nabla \cdot G\nabla \mathbf{u}'_j + \nabla(\lambda + G)\nabla \cdot \mathbf{u}'_j = -\rho\omega^2 \mathbf{u}'_j - \nabla \cdot \frac{\partial G}{\partial E_{z_j}} \nabla \mathbf{u}$$

$$- \nabla \frac{\partial}{\partial E_{z_j}} (\lambda + G)\nabla \cdot \mathbf{u}, \quad [7b]$$

where $\mathbf{u}'_j = \partial \mathbf{u}/\partial E_{z_j}$, has the identical form of Eq. [6a] in the quantity $\mathbf{u}'_j$ except for the occurrence of two additional right-hand-side quantities expressed in terms of $\mathbf{u}$. Because Eq. [5b] is evaluated at the current property estimate, $\mathbf{u}$ can be computed through Eq. [6a] leaving $\mathbf{u}'_j$ as the only unknown in Eq. [7b]. Evaluation of the terms expressing the differentiation of the elastic property distribution with respect to its parameterization, $\partial G/\partial E_{z_j}$, is facilitated by expanding the elastic constants in the finite element basis so that $E = \Sigma_{j=1}^{M_z} E_{z_j}\phi_j$. The finite element discretization of Eq. [7b] is described in further detail in the Appendix.

In practice, the subzone inversion algorithm begins with an initial estimate of the elastic property distribution, E^0, defined over the entire problem space, Ω. From this estimate, a global displacement field, $\mathbf{u}^c$, is computed from Eq. [6a] with the finite element method based on known displacement conditions from the MR data set, $\mathbf{u}^m$, applied along the global boundary, Γ. The squared error between the resulting displacement solution and the measured MR data is then calculated for each element. By using this error metric, an hierarchical list of element centroids is generated in which the element order is based on a decreasing squared-error contribution. A subzone domain, Ω_z, is then formed about an element centroid in the list by including all nearby elements whose centroids are within a user-defined radial distance from the subzone center. Figure 2 shows an example of a simple global finite element mesh with a close-up view of a single subzone that has been extracted for illustrative purposes. Once the subzone has been identified, a displacement field is calculated on the subzone by using the latest property parameter estimate, E_z^n, and the MR displacement information on the subzone boundary, Γ_z, as the boundary conditions required for finite element solution. The subzone property distribution is iteratively updated with the inversion process embodied in Eq. [5b] until a local convergence criterion between the computed and measured displacements internal to the subzone has been reached. At this point, the next element centroid in the error contribution list having participated in the fewest inversion operations is used to define another subzone, and the process of local convergence in the displacement field between computed and measured quan-
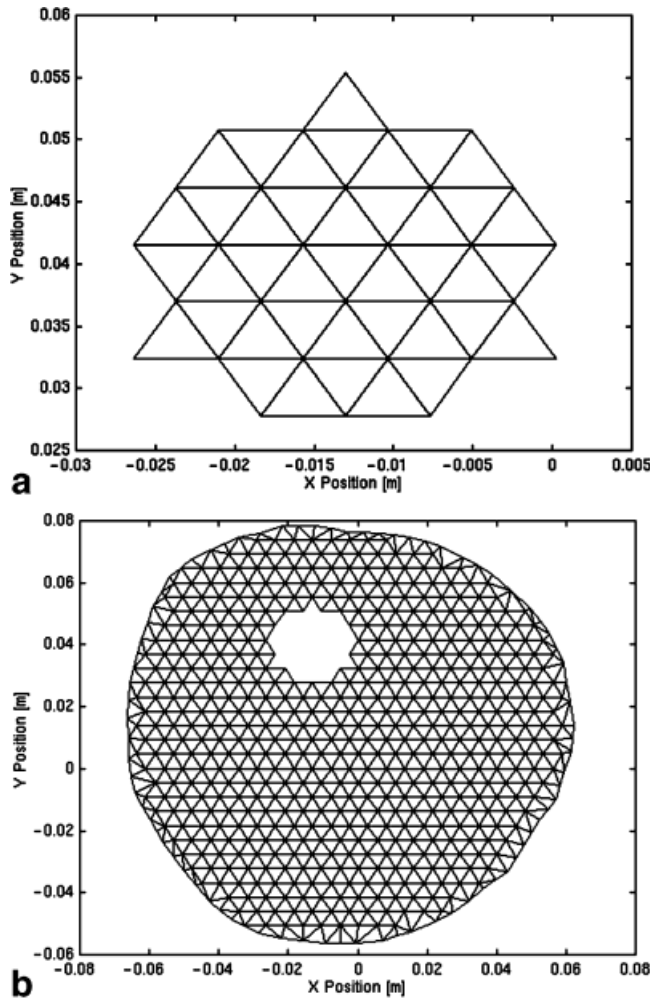
FIG. 2. Illustration of the mesh-based subzone technique in which a single subzone (**a**) has been extracted from a global finite element mesh (**b**).

tities is repeated. The zoning process continues until every element in the global mesh has been iterated a minimum number of times. The subzone solutions then end, another global displacement field calculation is executed with the latest property profile, and the zoning procedure begins again. Figure 3 illustrates the overall image reconstruction process.

RESULTS

Initial evaluations of the zoning algorithm have been performed on various numerical simulations of the displacement patterns generated in vibrating tissue. For these experiments, synthetic data were produced with the finite element method displacement calculation described in the Appendix. The mesh geometries were developed from MR images taken from actual patients, one being a modified anatomically coronal breast slice and the other a coronal brain image. For simplicity, we have assumed that the only unknown elastic parameter is Young's modulus, although this is not an inherent limitation in our algorithmic approach per se. Values for tissue density and Poisson's ratio were prescribed as 1020 kg/cm^3 and 0.49, respectively. The small wavelengths that develop in soft tissue (a Young's modulus of 8000 Pa was used for the background tissue value here) require that the planar MR image be divided into a large number of elements to ensure that the wave propagation is adequately well resolved. For example, the mesh used for the breast geometry consisted of 16,555 nodes and 32,635 linear triangular elements, resolving the tissue continuum to approximately 0.8 mm. The wavelength of a 100-Hz shear wave in this case is 1.62 cm/cycle, so this resolution provides approximately 18 or 19 nodes per mechanical wavelength. For synthetic data production, a spatial elasticity distribution is required. We have generated property distributions by thresholding MR images that contain either an arbitrary, user-defined elasticity map, as shown in Figure 4a, or one that follows tissue substructures that are identifiable in the MR image, as represented
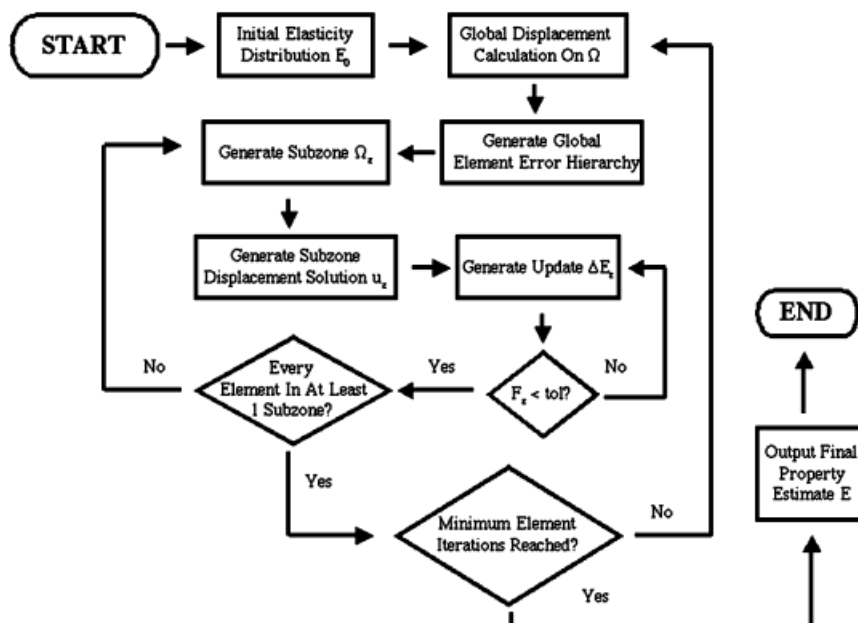

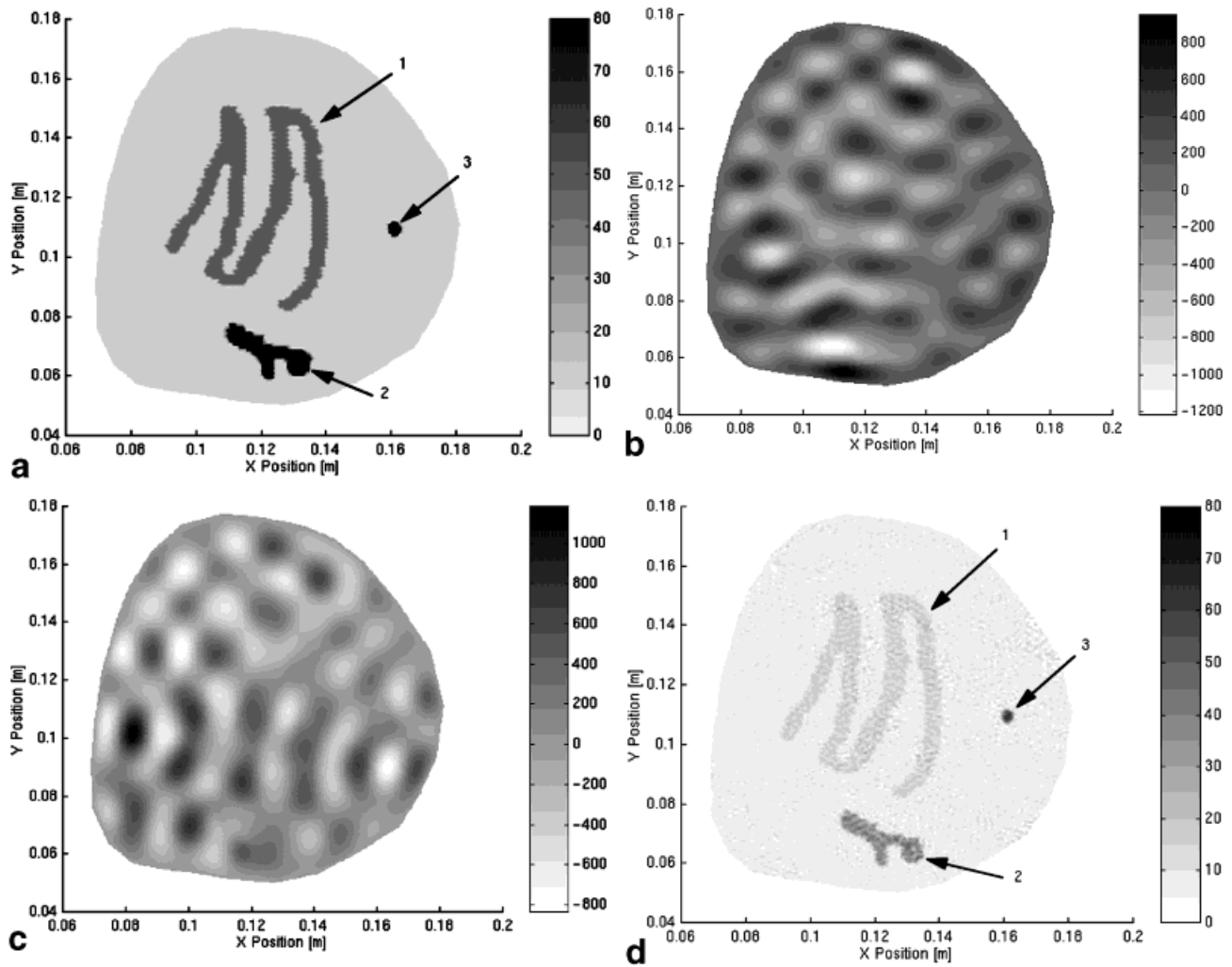FIG. 3. Flowchart of the subzone inversion algorithm.

FIG. 4. Breast elasticity problem consisting of an artificial property distribution containing three heterogeneities of increasing contrast with the background. **a:** Exact Young's modulus distribution (kPa), which includes three heterogeneities, designated as objects 1, 2, and 3. **b:** Synthetic *x*-direction displacement magnitude [μm]. **c:** Synthetic *y*-direction displacement magnitude [μm]. **d:** Reconstructed Young's modulus distribution (kPa) in the presence of 15% measurement noise.

in Figure 5a. Before inversion, a certain percentage of random noise is added to the synthetic data to simulate signal degradation that will occur in practice. This noise is generated by scaling the average displacement with a random number up to a given percentage and adding or subtracting that value from the original displacement at a particular node. The noisy solution is then used by the inversion algorithm described above as the measured data set.

For the breast case, an elasticity distribution was created that provided challenging inclusion geometries as well as a variety of inclusion stiffnesses. The background tissue stiffness was assigned a Young's modulus of 8000 Pa, which is believed to be at the lower end of actual soft tissue values (8,9,33). Inclusion stiffness ranges were determined as multiples (2× for object 1, 5× for object 2 and 10× for object 3 in Fig. 4a) of the background stiffness to test the contrast resolution of the numerical algorithm. The stiffest of the inclusions (object 3 in Fig. 4a) is roughly 4 mm in diameter, representing a very small tumor within the tissue. Once the stiffness information has been formulated for the forward problem, boundary conditions of 100 Hz

and 10 μm sinusoidal displacements are applied and the displacement solution is generated, shown here as *x* and *y* displacement magnitudes in Fig. 4b and c, respectively. Note the complex nature of this displacement pattern. For the small wavelengths expected in soft tissue, these complex displacement fields could lead to difficulties in generating property distributions based on direct interpretation of the displacement or strain image. The property inversion shown in Fig. 4d was generated by using synthetic data with 15% added noise with an initial guess of a uniform Young's modulus of 7000 Pa. The inversion process consisted of 18 sweeps over the entire space, each sweep involving roughly 1000 subzones of approximately 150 elements and 100 nodes each to ensure that every node was operated on at least once.

To demonstrate the ability of the algorithm to process realistic geometries generated from MR images, an elasticity distribution was reconstructed on a mesh generated from a coronal brain slice with two simulated inclusions as shown in Fig. 5a. To ensure accurate resolution, this mesh consisted of 19,446 nodes and 38,332 linear triangular elements. For this tissue, a background Young's modulus of
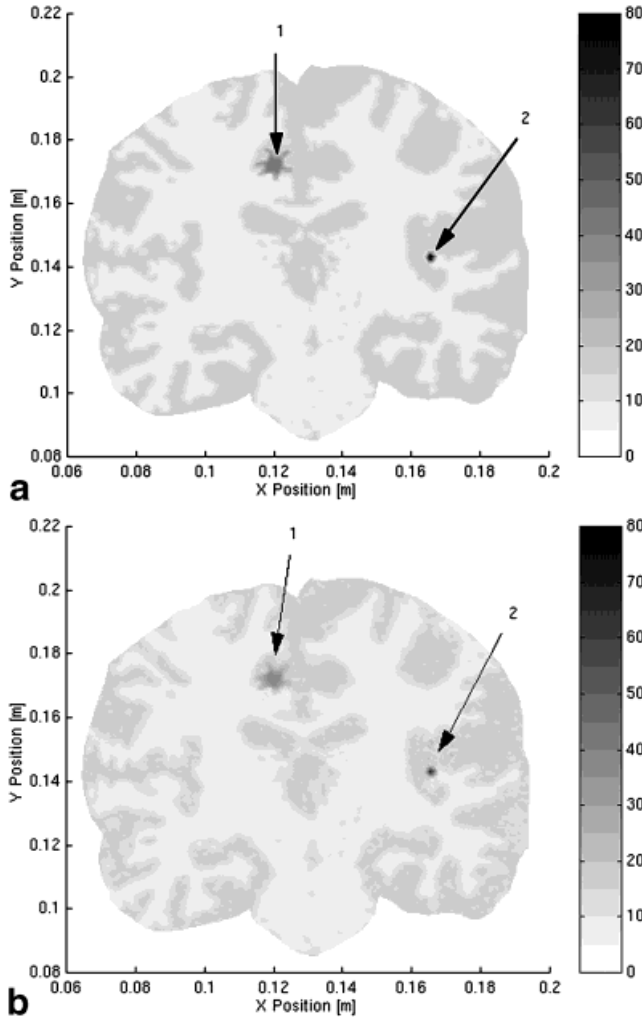
FIG. 5. Brain elasticity problem consisting of a property distribution derived from white/gray matter segmentation of a coronal MR image. **a:** Exact Young's modulus distribution (kPa) of the white/gray matter background with two artificially placed stiff anomalies designated as objects 1 and 2. **b:** Reconstructed Young's modulus distribution (kPa) in the presence of 15% measurement noise.

8000 Pa was used (33), representing the white matter, while the gray matter was assumed to be twice as stiff. The larger inclusion (designated as object 1 in Fig. 5a) measures approximately 1 cm and was assigned a stiffness five times that of the white matter, whereas the smaller inclusion (designated as object 2 in Fig. 5a) is roughly 4 mm in diameter and was specified as being an order of magnitude stiffer than white matter. The inversion process was completed in six global sweeps of 1240 subzones on average, with approximately 164 elements and 100 nodes in each zone. Figure 5b shows the recovered property distribution in the presence of 15% added noise; which compares very favorably with the exact distribution contained in Fig. 5a. A small degree of spatial filtering was found to be helpful in achieving a convergent solution in this case of high noise (34). This technique works to average the local property value at node i with the values at its immediately adjacent nodes so that $E_i^{new} = (1 - \theta)E_i^{old} + \theta/N_i \sum_{j=1}^{N_i} E_j^{old}$, where N_i is the number of neighbor nodes connected to

node i. For the inversion shown in Fig. 5b, a value of 0.2 was used for θ. Note that no spatial filtering was used (i.e., $\theta = 0$) during the inversion shown in Fig. 4d.

CONCLUSIONS

The image reconstructions presented in Figs. 4 and 5 show that the zoned inversion scheme is able to generate accurate Young's modulus distribution images on the basis of displacement information obtained in the presence of high noise (up to 15%). The zoned inversion method also allows for a high degree of parameter discretization, taking full advantage of the data-rich nature of an MR displacement image. This high resolution allowed the inversion routine to discern hard inclusions as small as 4 mm in diameter during simulation. Although there are additional complexities associated with the inversion of actual MR data, these promising simulation results suggest that the subzone technique should provide a powerful framework for recovering elasticity distributions with MR elastography. Specifically, it provides a computationally viable approach that capitalizes on the MR measurement density to yield high-resolution (pixel-level) tissue property maps. The complex nature of the displacement fields that develop in soft tissue makes an imaging algorithm that exploits modeling concepts essential. Use of the finite element method allows the incorporation of tissue mechanics into the analysis of measured displacement patterns so that the complicated waveforms inherent in multidimensional elastic systems may be taken into account.

The finite element inversion process also provides some important avenues for dealing with noisy data and more complicated physical models. The iterative inversion scheme detailed here is amenable to a total variation minimization process, which can be useful in reducing the effects of noise degradation (35). Work is also under way to incorporate a Maxwellian damping term into the inversion process so that tissue-damping effects can be both accounted for and measured in the same manner that Young's modulus is recovered with the algorithm detailed here. Furthermore, the process should be adaptable to modeling transient motion rather than using a steady-state assumption if steady-state data sets cannot be obtained from the MR. In summary, this zoned finite element inversion technique provides a powerful method for deriving highly resolved Young's modulus distribution information in a way that is robust in the presence of high noise and adaptable to a variety of modifications that could improve its performance in the future.

APPENDIX

Here we describe the finite element formulation of the forward and inverse problems in more detail. The governing equation of linear elasticity, Eq. [6a], is cast in terms of the Cauchy stress tensor, $\mathscr{T}$, which leads more readily to the 2D plane stress or plane strain conditions assumed for the forward and inverse solutions presented.

The Forward Problem

If steady-state harmonic motion is assumed, the real valued displacement vector solution can be represented as the real part of a complex-valued, spatially varying displacement phasor multiplied by the complex exponential

$$\mathbf{u}(x, y, t) = Re[\overline{\mathbf{u}}(x, y)e^{i\omega t}], \qquad [8]$$

where spatial coordinates x and y and complex displacement components u and v define

$$\overline{\mathbf{u}}(x, y) = \begin{Bmatrix} u \\ v \end{Bmatrix}. \qquad [9]$$

In stress tensor notation, the harmonic equilibrium condition will then be (36)

$$\nabla \cdot \mathscr{T} = -\rho\omega^2\overline{\mathbf{u}} + \mathbf{F}, \qquad [10]$$

making use of the complex harmonic inertia, $\rho\partial^2\mathbf{u}/\partial t^2 = -\rho\omega^2 \overline{\mathbf{u}}e^{i\omega t}$, and including any additional body forces $\mathbf{F}$ that may be present. The stress tensor $\mathscr{T}$ can be defined as

$$\mathscr{T} = \hat{\mathbf{i}}\tau_{\mathbf{x}} + \hat{\mathbf{j}}\tau_{\mathbf{y}} + \hat{\mathbf{k}}\tau_{\mathbf{z}}$$

$$\tau_{\mathbf{x}} = \hat{\mathbf{i}}\sigma_x + \hat{\mathbf{j}}\tau_{xy} + \hat{\mathbf{k}}\tau_{xz}$$

$$\tau_{\mathbf{y}} = \hat{\mathbf{i}}\tau_{yx} + \hat{\mathbf{j}}\sigma_y + \hat{\mathbf{k}}\tau_{yz}$$

$$\tau_{\mathbf{z}} = \hat{\mathbf{i}}\tau_{zx} + \hat{\mathbf{j}}\tau_{zy} + \hat{\mathbf{k}}\sigma_{z},$$

and for 2D plane strain or plane stress assumptions the stress-strain relations for elastic solids can be written in the matrix form

$$\begin{Bmatrix} \sigma_x \\ \sigma_y \\ \tau_{xy} \end{Bmatrix} = E \cdot \mathscr{E}_1 \begin{bmatrix} 1 & \mathscr{E}_2 & 0 \\ \mathscr{E}_2 & 1 & 0 \\ 0 & 0 & \dfrac{\mathscr{G}}{\mathscr{E}_1} \end{bmatrix} \begin{Bmatrix} \dfrac{\partial u}{\partial x} \\ \dfrac{\partial v}{\partial y} \\ \dfrac{\partial u}{\partial y} + \dfrac{\partial v}{\partial x} \end{Bmatrix}, \qquad [11]$$

with

$$\mathscr{E}_1 = \frac{1-\nu}{(1+\nu)(1-2\nu)} \text{ (plane strain) or } \frac{1}{1-\nu^2} \text{ (plane stress)}$$

$$\mathscr{E}_2 = \frac{\nu}{1-\nu} \text{ (plane strain) or } \nu \text{ (plane stress)}$$

$$\mathscr{G} = \frac{1}{2(1+\nu)},$$

where E is Young's modulus.

To facilitate the solution of this set of equations for complicated geometries containing realistic property distributions, a finite element discretization method is adopted where $\hat{\mathbf{u}}$, the approximate solution to the displacement magnitude $\overline{\mathbf{u}}$, is expanded on a set of locally active, spatially varying Lagrangian basis functions, ϕ_j, so that

$$\hat{u} = \sum_{j=1}^{N} u_j\phi_j, \text{ and } \hat{v} = \sum_{j=1}^{N} v_j\phi_j, \qquad [12]$$

where u_j and v_j are the approximate x and y directed displacements at the jth of N nodes. Developing a Galerkin weak form of Eq. [10] generates the system of equations

$$[\mathbf{A}]\begin{Bmatrix} \hat{u} \\ \hat{v} \end{Bmatrix} = [\mathbf{b}], \qquad [13]$$

with matrix $[\mathbf{A}]$ consisting of the subelements

$$[a_{i,j}] = \begin{bmatrix} \alpha_{11} & \alpha_{12} \\ \alpha_{21} & \alpha_{22} \end{bmatrix} \qquad [14]$$

where

$$\alpha_{11} = \left\langle \frac{\partial\phi_i}{\partial x}\frac{\partial\phi_j}{\partial x} E \cdot \mathscr{E}_1 + \frac{\partial\phi_i}{\partial y}\frac{\partial\phi_j}{\partial y} E \cdot \mathscr{G} - \rho\omega^2\phi_i\phi_j \right\rangle$$

$$\alpha_{12} = \left\langle \frac{\partial\phi_i}{\partial x}\frac{\partial\phi_j}{\partial y} E \cdot \mathscr{E}_1\mathscr{E}_2 + \frac{\partial\phi_i}{\partial y}\frac{\partial\phi_j}{\partial x} E \cdot \mathscr{G} \right\rangle$$

$$\alpha_{21} = \left\langle \frac{\partial\phi_i}{\partial y}\frac{\partial\phi_j}{\partial x} E \cdot \mathscr{E}_1\mathscr{E}_2 + \frac{\partial\phi_i}{\partial x}\frac{\partial\phi_j}{\partial y} E \cdot \mathscr{G} \right\rangle$$

$$\alpha_{22} = \left\langle \frac{\partial\phi_i}{\partial y}\frac{\partial\phi_j}{\partial y} E \cdot \mathscr{E}_1 + \frac{\partial\phi_i}{\partial x}\frac{\partial\phi_j}{\partial x} E \cdot \mathscr{G} - \rho\omega^2 \phi_i\phi_j \right\rangle,$$

and the column vectors of unknown nodal displacements and right-hand-side forcing being written as

$$\begin{Bmatrix} \hat{u} \\ \hat{v} \end{Bmatrix} = [\hat{\mathbf{u}}] = \{\hat{u}_1, \hat{v}_1, \hat{u}_2, \hat{v}_2, \ldots, \hat{u}_N, \hat{v}_N\}^T, \qquad [15]$$

and

$$b_i = \begin{Bmatrix} \hat{\mathbf{x}} \cdot [\oint\mathscr{T}\cdot \hat{\mathbf{n}}\phi_i ds - \langle \mathbf{F}\phi_i\rangle] \\ \hat{\mathbf{y}} \cdot [\oint\mathscr{T}\cdot \hat{\mathbf{n}}\phi_i ds - \langle \mathbf{F}\phi_i\rangle] \end{Bmatrix} \qquad [16]$$

for i and j running from 1 to N.

The Inverse Problem

For the inversion problem, the basis set used to expand the parameterized elasticity solution is taken to be the same finite element basis set used to expand the displacement solution $\hat{\mathbf{u}}$. The calculation of the $\partial\mathbf{u}/\partial E$ terms needed to generate the Hessian matrix and the right-hand-side vector $\mathbf{f}$ in Eq. [5b] is then achieved directly by the differentiation of Eq. [13], the discretized version of Eq. [10], with respect

to E, leading to

$$\frac{\partial \hat{\mathbf{u}}}{\partial E_k} = -[\mathbf{A}]^{-1} \frac{\partial \mathbf{A}}{\partial E_k} \cdot \hat{\mathbf{u}}, \qquad [17]$$

where $\partial \mathbf{A}/\partial E_k$ has terms

$$\left[\frac{\partial a_{i,j}}{\partial E_k}\right] = \begin{bmatrix} \dfrac{\partial \alpha_{11}}{\partial E_k} & \dfrac{\partial \alpha_{12}}{\partial E_k} \\[2mm] \dfrac{\partial \alpha_{21}}{\partial E_k} & \dfrac{\partial \alpha_{22}}{\partial E_k} \end{bmatrix} \qquad [18]$$

with

$$\frac{\partial \alpha_{11}}{\partial E_k} = \left\langle \frac{\partial \phi_i}{\partial x} \frac{\partial \phi_j}{\partial x} \phi_k \mathscr{E}_1 + \frac{\partial \phi_i}{\partial y} \frac{\partial \phi_j}{\partial y} \phi_k \mathscr{G} \right\rangle$$

$$\frac{\partial \alpha_{12}}{\partial E_k} = \left\langle \frac{\partial \phi_i}{\partial x} \frac{\partial \phi_j}{\partial y} \phi_k \mathscr{E}_1 \mathscr{E}_2 + \frac{\partial \phi_i}{\partial y} \frac{\partial \phi_j}{\partial x} \phi_k \mathscr{G} \right\rangle$$

$$\frac{\partial \alpha_{21}}{\partial E_k} = \left\langle \frac{\partial \phi_i}{\partial y} \frac{\partial \phi_j}{\partial x} \phi_k \mathscr{E}_1 \mathscr{E}_2 + \frac{\partial \phi_i}{\partial x} \frac{\partial \phi_j}{\partial y} \phi_k \mathscr{G} \right\rangle$$

$$\frac{\partial \alpha_{22}}{\partial E_k} = \left\langle \frac{\partial \phi_i}{\partial y} \frac{\partial \phi_j}{\partial y} \phi_k \mathscr{E}_1 + \frac{\partial \phi_i}{\partial x} \frac{\partial \phi_j}{\partial x} \phi_k \mathscr{G} \right\rangle$$

REFERENCES

1. Parker KJ, Gao L, Lerner RM, Levinson SF. Techniques for elastic imaging: a review. IEEE Eng Med Biol Mag 1996;15:52–59.
2. Muthupillai R, Rosman PJ, Greenleaf JF, Manduca A, Ehman RL. Magnetic resonance elastography by direct visualization of propagating acoustic strain waves. Science 1995;269:1854–1857.
3. Davies BL, Harris SJ, Lin WJ, Hibberd RD, Middleton R, Cobb JC. Active compliance in robotic surgery: the use of force control as a dynamic constraint. Proc Inst Mech Eng [H] 1997;211:285–292.
4. Delp SL, Stulberg SD, Davies B, Picard F, Leitner F. Computer assisted knee replacement. Clin Orthop Rel Res 1998;354:49–56.
5. Miga MI, Paulsen KD, Hoopes PJ, Kennedy FE, Hartov A, Roberts DW. In-vivo quantification of a homogeneous brain deformation model for updating preoperative images during surgery. IEEE Trans Biomed Eng 1999, in press.
6. Paulsen KD, Miga MI, Kennedy FE, Hoopes PJ, Hartov A, Roberts DW. A computational model for tracking subsurface tissue deformation during stereotactic neurosurgery. IEEE Trans Biomed Eng 1999;46:213–225.
7. Roberts DW, Miga MI, Hartov A, Eisner S, Lemory J, Kennedy FE, Paulsen KD. Intraoperatively updated neuroimaging using brain modeling and sparse data. Neurosurgery 1999, in press.
8. Fung YC. Biomechanics; mechanical properties of living tissues, 2nd ed. New York: Springer-Verlag; 1993.
9. Park JB. Biomaterials science and engineering. New York: Plenum; 1984.
10. Céspedes I, Ophir J, Ponnekanti H, Maklad N. Elastography: elasticity imaging using ultrasound with application to muscle and breast in-vivo. Ultrason Imaging 1993;15:73–88.
11. Gao L, Parker KJ, Alam SK, Lerner RM. Sonoelasticity imaging: theory and experimental verification. J Acoust Soc Am 1995;97:3875–3886.
12. Kallel F, Ophir J. A least-squares strain estimator for elastography. Ultrason Imaging 1997;19:195–208.
13. Lerner RM, Huang SR, Parker KJ. ''Sonoelasticity'' images derived from ultrasound signals in mechanically vibrated tissues. Ultrasound Med Biol 1990;16:231–239.
14. Nicholas D, Nassiri DK, Garbutt P, Hill CR. Tissue characterization from ultrasound B-scan data. Ultrasound Med Biol 1986;12:135–143.
15. Ophir J, Céspedes I, Ponneckanti H, Yazdi Y, Li X. Elastography: a quantitative method for imaging the elasticity of biological tissues. Ultrason Imaging 1991;13:111–134.
16. Yamakoshi Y, Sato J, Sato T. Ultrasonic imaging of internal vibration of soft tissue under forced vibration. IEEE Trans Ultrason Ferroelectrics Frequency Control 1990;37:45–53.
17. Gao L, Alam SK, Parker KJ. A new vibration theory for sonoelasticity imaging. In: Proceedings of the IEEE Ultrasonics Symposium, Baltimore, 1993. p. 879–882.
18. Kallel F, Bertrand M. Tissue elasticity reconstruction using linear perturbation method. IEEE Trans Med Imaging 1996;15:299–313.
19. Skovoroda AR, Emelianov SY, Lubinski MA, Sarvazyan AP, O'Donnell M. Theoretical analysis and verification of ultrasound displacement and strain imaging. IEEE Trans Ultrason Ferroelectrics Frequency Control 1994;41:302–313.
20. Bishop J, Poole G, Leitch M, Plewes DB. Magnetic resonance imaging of shear wave propagation in excised tissue. J Magn Reson Imaging 1998;8:1257–1265.
21. Lewa CJ. Magnetic resonance imaging in the presence of mechanical waves. Spectrosc Lett 1991;24:55–67.
22. Muthupillai R, Rossman PJ, Lomas DJ, Greenleaf JF, Riederer SJ, Ehman RL. Magnetic resonance imaging of transverse acoustic strain waves. Magn Reson Med 1996;36:266–274.
23. Chenevert TL, Skovoroda AR, O'Donnell M, Emelianov SY. Elasticity reconstructive imaging by means of stimulated echo MRI. Magn Reson Med 1998;39:482–490.
24. Raghavan KR, Yagle AE. Forward and inverse problems in elasticity imaging of soft tissues. IEEE Trans Nucl Sci 1994;41:1639–1648.
25. Lewa CJ, De Certaines JD. Viscoelastic property detection by elastic displacement NMR measurements. J Magn Reson Imaging 1996;6:652–656.
26. Manduca A, Muthupillai R, Rossman PJ, Greenleaf JF, Ehman RL. Image processing for magnetic resonance elastography. SPIE 1996;2710:616–623.
27. Sumi C, Nakayama K. A robust numerical solution to reconstruct a globally relative shear modulus distribution from strain measurements. IEEE Trans Med Imaging 1998;17:419–428.
28. Paulsen KD, Moskowitz MJ, Ryan TP. Temperature field estimation using electrical impedance profiling methods. I. Reconstruction algorithm and simulated results. Int J Hyperthermia 1994;10:209–228.
29. Paulsen KD, Jiang H. Spatially varying optical property reconstruction using a finite element diffusion equation approximation. Med Phys 1995;22:691–701.
30. Paulsen KD, Jiang H. An enhanced electrical impedance imaging algorithm for hyperthermia applications. Int J Hyperthermia 1997;13:459–480.
31. Press WH, Flannery BP, Teukolsky SA, Vetterling WT. Numerical recipes; the art of scientific computing. New York: Cambridge University Press, 1986. Section 14.4.
32. Marquardt DW. An algorithm for least-squares estimation of nonlinear parameters. SIAM J Appl Math 1963;11:431–441.
33. Nagashima T, Shirakuni T, Rapoport SI. A two-dimensional, finite element analysis of vasogenic brain edema. Neurol Med Chir (Tokyo) 1990;30:1–9.
34. Jiang H, Paulsen KD, Osterberg UL, Pogue BW, Patterson MS. Optical image reconstruction using frequency domain data: simulations and experiments. J Opt Soc Am A 1996;13:253–266.
35. Paulsen KD, Jiang H. Enhanced frequency-domain optical image reconstruction in tissues through total-variation minimization. Appl Opt 1996;35:3447–3458.
36. Chou PC, Pagano NJ. Elasticity; Tensor, Dyadic and Engineering Approaches. New York: Dover Publications; 1967.